DISTRIBUTION STATEMENT A
Approved for Public Release
Distribution Unlimited

A TE_{11} K_a-Band Gyro-TWT Amplifier With High-Average Power Compatible Distributed Loss

Dean E. Pershing, Khanh T. Nguyen, Jeffrey P. Calame, *Member, IEEE*, Bruce. G. Danly, Baruch Levush, *Fellow, IEEE*, Franklin N. Wood, and M. Garven

***Abstract*—Current amplifier research at the Naval Research Laboratory Vacuum Electronics Branch emphasizes techniques to extend the bandwidth and average power capability of gyro devices for millimeter wave radar applications. This paper will discuss the implementation of a wideband high-gain gyro-traveling wave tube amplifier design, with a measured peak output power of 78 kW, gain ~60 dB, and a 3-dB bandwidth of 4.2 GHz (12%) at 52 kW in K_a-band. The 3-dB saturated bandwidth at 70 kW is 6 GHz (17%), which is also the instantaneous bandwidth with appropriately tailored input power (e.g., gain equalizer). The amplifier operates in the TE_{11} mode and for stabilization employs a high-average power compatible diffractive loading technique.**

***Index Terms*—Dielectric, gyro-traveling wave tube (gyro-TWT), loss, millimeter-wave amplifier.**

I. Introduction

HISTORICALLY, spurious oscillations have been a major obstacle in realizing full gyro-traveling wave tube (gyro-TWT) potential. Use of distributed loss in gyro-TWTs Chu *et al.* [1] (also [2]) marked a major advancement in the suppression of spurious oscillations, thus permitting high gain and power operation. A summary of recent experimental gyro-TWTs employing distributed loss is given in [3]. Note that other stabilization techniques also show promise, such as that reported by Denisov *et al.* [4] in which the waveguide dispersion characteristics of a helically grooved waveguide are advantageously employed to reduce sensitivity to oscillations and increase efficiency. Most distributed loss stabilized gyro-TWTs to date have employed a thin lossy coating that is not compatible with high-average power operation. The project emphasis at the Naval Research Laboratory (NRL) has been on distributed loss stabilized gyro-TWTs with high-average power capability. In addition to the amplifier described here, a different distributed loss technique [5] has been successfully employed in a TE_{01} gyro-TWT amplifier at NRL [6]. The component design and initial experimental results for a TE_{11} K_a-band gyro-TWT amplifier employing a unique distributed loss approach are described below.

Manuscript received September 12, 2003; revised December 1, 2003. This work was supported by the Office of Naval Research (ONR) and the Naval Research Laboratory (NRL).

D. E. Pershing, F. N. Wood, and M. Garven are with the Vacuum Electronics Branch, U.S. Naval Research Laboratory, Washington, DC 20375 USA and also with the Mission Research Corporation, Newington, VA 22122 USA (e-mail: pershing@estd.nrl.navy.mil; fwood@estd.nrl.navy.mil; garven@ccf.nrl.navy.mil).

K. T. Nguyen is with the Vacuum Electronics Branch, U,S. Naval Research Laboratory, Washington, DC 20375 USA and also with Beam-Wave Research, Inc., Silver Spring, MD 20905 USA (e-mail: knguyen@estd.nrl.navy.mil).

J. P. Calame, B. G. Danly, and B. Levush are with the Vacuum Electronics Branch, U.S. Naval Research Laboratory, Washington, DC 20375 USA (e-mail: calame@estd.nrl.navy.mil; danly@estd.nrl.navy.mil; levush@estd.nrl.navy.mil).

Digital Object Identifier 10.1109/TPS.2004.828823

II. Experimental Design

Details of the amplifier physics design are given in [7], but a summary of the major design issues is given here. Given the accelerating voltage and desired frequency range, gain, and output power, the various tradeoffs for the interaction region can be explored. The lengths of the loaded and unloaded sections of the interaction circuit are selected to satisfy stability constraints, overall amplifier gain, and efficiency requirements. The loss section needs to be sufficiently long and with sufficient loss for the desired gain and zero-drive stability, but not too long or velocity spread will compromise performance. It must especially load the spurious modes. In our case, the loss design must also be high-average power capable. A short unloaded section is added for nonlinear gain and high power. Its length must be less than the critical length for start oscillation in the given magnetic field. A too long section will also compromise bandwidth due to beam velocity spread.

The appropriate magnetic field must be chosen for near grazing to slightly above grazing with the waveguide mode for the given waveguide size and beam voltage. The magnetic field is tapered where possible in regions of uniform diameter waveguide in order to ensure no oscillations. For this design, the field is tapered at the input coupler and at the output at the unloaded section and uptaper. A nonlinear uptaper is used to couple RF from the interaction circuit to the outside world with miminal reflection of the operating mode and minimal conversion to other modes. For each set of beam and field values, the RF input power is chosen for flattest response. The implementation of these design considerations is described below. The wall geometry, magnetic field profile, and calculated power for this amplifier design are shown in Fig. 1 for the operational parameters: Vb = 70 kV, Ib = 6 A, Rg = 1.21 mm, Bz = 12.1 kG. Stability considerations require the following loss rates for this amplifier design: TE_{11}: 3.45 dB/cm @ 35 GHz (attenuation versus frequency profile is approximately inversely proportional to TE_{11} group velocity) TE_{21}: 4.25 dB/cm @ 56 GHz.

A. Experimental Setup

A schematic of the experimental setup is shown in Fig. 2, with the following major components: electron gun, input

0093-3813/04$20.00 © 2004 IEEE

20050112 047

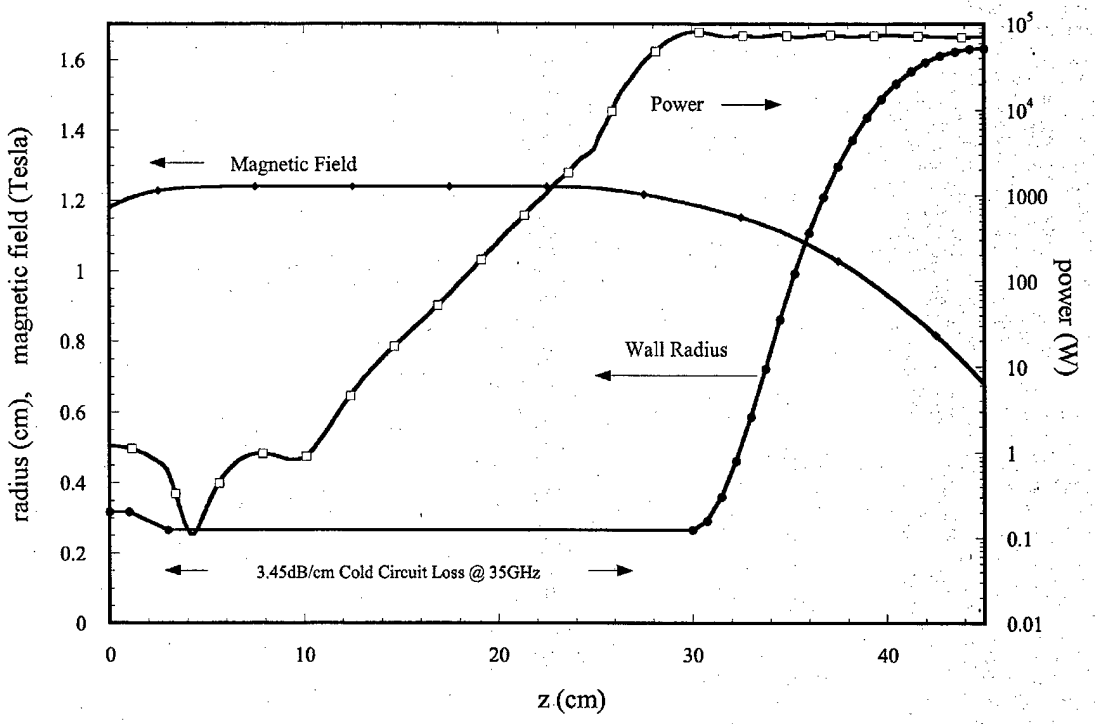

Fig. 1. Circuit geometry, magnetic field profile, and calculated spatial power profile for this amplifier. Operational parameters are: Vb = 70 kV, Ib = 6 A, Rg = 1.21 mm, Bz = 12.1 kG.

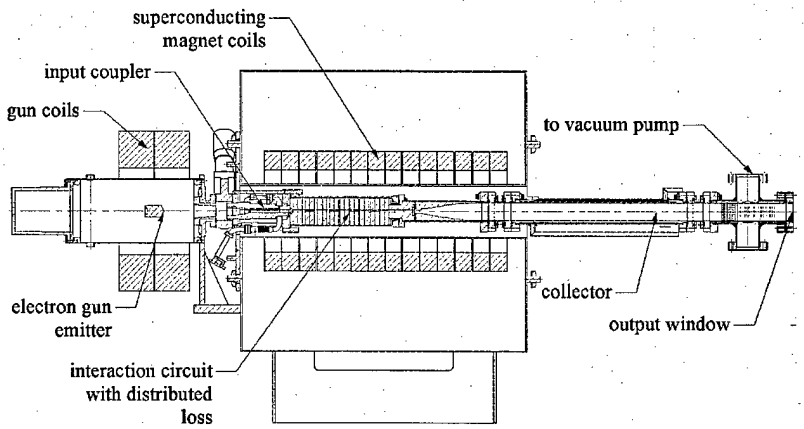

Fig. 2. Schematic diagram of the NRL TE_{11} K_a-band gyro-TWT amplifier.

coupler, interaction circuit employing distributed loss, and broadband output window. In order to demonstrate the amplifier performance potential, several component design challenges had to be met. While listed in order of placement in the device, the most important is the interaction circuit. The electron gun is required to generate a high-current gyrating beam with low velocity spread and small guiding center. The input coupler is designed to generate a circularly polarized TE_{11} wave for maximum power transfer from source to interaction region over a frequency range of 33–39 GHz with tight coupling (~1 dB) and short axial length. The interaction circuit must achieve the desired loss rates for the TE_{11} operating mode and for the TE_{21} spurious mode, and with a loss mechanism that is high-average power compatible. The output window must operate over a 33–39-GHz bandwidth with low reflection for both TE_{11} and TE_{21} modes.

The RF signal path is as follows. An HP 83650A synthesized sweeper is used to drive a Hughes 10-W instrumentation helix TWTA through a variable attenuator. The TWTA output then drives a magic T connected to both delay section arms of the input coupler if circular polarization is desired. For linear polarization, the magic T is removed and the TWTA drives one arm of the delay section with the other arm terminated.

An output coupler is not used to measure gyro-TWT output power. The full amplified power is radiated into an anechoic chamber with a small fraction (~ −30 dB) sampled by a spaced pickup waveguide. Power is further attenuated by an additional 30 dB using a calibrated directional coupler and variable atten-

uator before detection by an HP 84814A peak power sensor/HP 8990A peak power analyzer. A second peak power sensor/analyzer combination is used to monitor the RF input power as well as power reflected from the input coupler.

The main magnetic field is generated using a superconducting solenoid with 14 individually adjustable coils, permitting fine control of the field profile. Two conventional water-cooled magnets are used to control the magnetic field at the gun.

Detailed descriptions of the major components are presented below.

B. Component Description

1) Input Coupler Design: The input coupler is designed to maximize power transfer from the driver to the interaction circuit over a 6-GHz bandwidth, 33–39 GHz. In order to maximize gain with limited input power, we want to launch a circularly polarized TE_{11} wave into the interaction region with a coupling factor as close to 0 dB as possible. The coupler length must not exceed the critical length for oscillations in the given magnetic field. Additionally, the coupler must absorb reflected power from the interaction circuit, as well as permitting the passage of the electron beam.

To generate a circularly polarized wave, we need to provide equal power in orthogonal polarizations with a 90° phase shift or delay. Since we must allow for an electron beam, designs that require RF input along the axis are not usable. We have chosen orthogonal multihole directional couplers as the basis for this design. The major elements of this coupler consist of a vacuum window, a power split/delay section, a rectangular to circular coupling section with loads for the coupling arms, and a packaging geometry consistent with space constraints.

A description of each element is given below, starting with the basic coupling configuration. We start with a linear polarization design with coupling between the narrow wall of a WR28 waveguide and a circular waveguide at the interaction radius. From an analytic calculation of multi-aperture coupling from rectangular to circular waveguides, a rough idea of the number of apertures, aperture size, and spacing can be determined. More detailed calculations of the coupling factor were made using HFSS [8]. Broader bandwidth is achieved by matching phase velocities with a slightly larger circular waveguide and smaller rectangular waveguide (WR-22). The final configuration consists of 14 rectangular apertures across the full height of the rectangular waveguide with three reduced-size apertures at either end of the array for matching. The circular-to-rectangular waveguide radial separation is ~0.5 mm. For circular polarization, two axial aperture arrays are placed 90° apart. Each rectangular waveguide is terminated with an integral AlN/SiC load. The calculated coupling factor is ~ -1 dB. The basic coupler geometry is shown in Fig. 3, along with a simulation result of power transfer from the TE_{10} rectangular mode to the TE_{11} circular mode.

The configuration described above launches two orthogonal, linearly polarized waves with relatively flat frequency response. For circular polarization, the coupling arms must be driven with equal power and with a 90° relative phase shift, independent of frequency. A commercial WR-28 magic T supplies the requisite power split with a 0° or 180° phase split operating in air. The delay section operates in vacuum following the vacuum

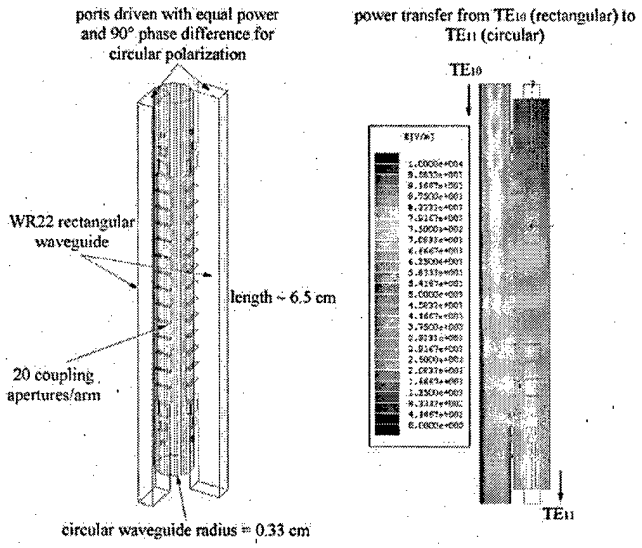

Fig. 3. Input coupler design: TE_{10} (rect.) to TE_{11} (circ. pol.).

windows and utilizes the different dispersion characteristics of WR-22 and WR-28 waveguide with a path length difference to give a broadband 90° phase shift between the input arms. This is achieved with a "jog" section of WR-28 waveguide with a 1.095 cm path length versus a 1.0-cm length of WR-22 waveguide. The "jog" section is used for equal linear (not path) lengths for each arm. Either right- or left-circular polarization can be launched with appropriate choice of E or H input to the magic T. Linear polarization input can also be generated with removal of the magic T and injection of power into either drive arm. It should be noted that a small degree of ellipticity is introduced even with exact 3-dB power split and 90° phase difference to the driving arms. There is approximately -19 dB of cross coupling due to the large aperture sizes. This translates to ~2%–6% of power conversion to the counter-rotating mode with the complete coupler assembly. Note that although considerable effort was devoted to design a broadband circular polarization input coupler with tight coupling, path length errors in manufacture severely compromised performance. True circular polarization was only obtained in a ~2-GHz range around 36 GHz. Given the flexibility of the design, however, linear polarization operation was also possible. The experimental data described was obtained using linear polarization input.

The final "feature" of this coupler design is the "plumbing" arrangement necessary to fit the drive arms within the length of the coupler body while simultaneously fitting between the magnet, gate valve, and electron gun. As shown in Fig. 4, the input arms wrap around the length of the coupler body.

2) Input Coupler Performance: Testing the assembled input coupler posed special challenges due to the mixture of waveguide types and polarizations, as well as the available diagnostic hardware. Two coupling factor calibration methods were used. First, an HP 8510 network analyzer measurement was performed using the output coupler from the NRL K_u-band Ubitron experiment [9] as a mode transformer from a linearly polarized TE_{11} circular mode to the TE_{10} rectangular mode. Second, a polarization insensitive water load/calorimeter was

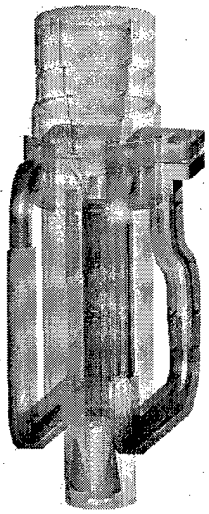

Fig. 4. Input coupler design details.

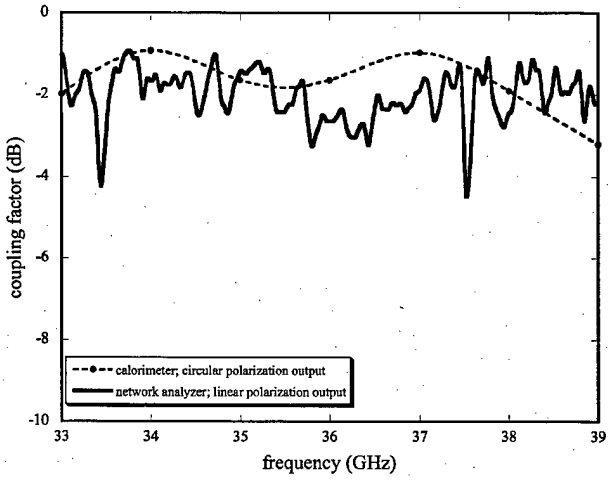

Fig. 5. Measured input coupler coupling factor.

used to measure the total power leaving the input coupler. Fig. 5 shows the measured input coupler characteristics under the two described conditions: single port excitation leading to linearly polarized output, and two port excitation with appropriate power/phase splits leading to circularly polarized output. The figure basically shows that the input coupler is broadband with reasonably tight coupling to the circular waveguide and indicates only 0.5–1-dB higher loss than calculated. It should be noted, that, due to unfortunate errors in fabrication of the delay section, the desired 90° phase difference could not be maintained over the entire 6-GHz bandwidth. As a consequence, most GTWT testing utilized linear polarization input to the interaction region.

3) Output Window Design: Since this amplifier is expected to operate over a frequency range of 33–39 GHz, the output window must present at least 20-dB return loss for the operating mode over this bandwidth. In addition, the window should also have better than 6-dB return loss at 56 GHz to reduce the possible occurrence of the second harmonic TE_{21} BWO. This latter requirement is not crucial, however, since this mode is highly attenuated by the distributed loss section.

Radial extraction of the output RF is not used for this amplifier, so the output window is inline with the circuit at the end of the beam collector. For broad bandwidth, it appears that a multiple dielectric resonant disk configuration is most suitable. To achieve a 6-GHz bandwidth we have chosen a triple quartz disk assembly with the vacuum window brazed to a titanium holder. Very good performance is possible if only the TE_{11} mode is considered. Including an additional requirement for low TE_{21} reflection at 56 GHz compromises performance of the window for the operating mode. However, an optimization procedure can be used to simultaneously satisfy the conflicting requirements, where the disk thicknesses and spacings are variables. Codes used in the design process include CASCADE [10], resonance [11], and HFSS.

Since the brazing procedure is somewhat unusual, a brief description is given here. The fabrication technique to provide a wideband ∅1.5-in waveguide window for this amplifier, which would satisfy the UHV requirements and allow the tube to be baked at ~400 °C was pursued. A review of vacuum sealing literature suggested a technique reported by Armand [12] to braze the edge of a fused silica ("quartz") disk directly to a cylindrical titanium holder. Brazing is accomplished using a silver-copper eutectic, MP 779 °C, at 850 °C in a vacuum of approximately 4.0×10^{-6} torr.

The cylindrical titanium holder with wall thickness of 0.050 in is machined with a tailored inside diameter at the fused silica interface and incorporates a conventional knife-edge for sealing to a standard ∅3.37 CF flange using a copper gasket.

Initial attempts to employ the above technique highlighted the importance of geometry and, in particular, the degree of interference. Since the coefficient of thermal expansion for titanium (commercially pure grade) is significantly larger than that for fused silica, 8.8×10^{-6}/°C Vs 5.5×10^{-7}/°C, respectively, the dimensions of the mating surfaces are critical. At room temperature an interference fit of 0.006 to 0.008 in on a diameter proved most reliable. A fixture was designed to position the disc over the titanium holder and to allow, upon heating to 950 °C, the disc to drop into position with a theoretical radial clearance of 0.0015 in. After checking for positional accuracy at room temperature, a single loop of ∅.020 braze alloy wire was placed at the window/holder interface. These parts were then reinserted into the vacuum furnace within the positioning fixture and heated to 850 °C. The typical minimum braze temperature for copper-silver eutectic (~800 °C is too low to allow sufficient titanium from the holder base metal to go into solution, wetting the window.

Window performance is very sensitive to both individual disk thicknesses as well as disk spacings. Due to fabrication and assembly tolerances, the actual window thicknesses are 0.0827, 0.0866, and 0.0866 in with disk separations of 0.0825 and 0.0842 in. The calculated return of this assembly for the TE_{11} and TE_{21} modes is shown in Fig. 6. Accurate measurements of window performance were not made, due to a lack of suitable diagnostic hardware and calibration standards. However, reflection measurements were made using the assembled nonlinear uptaper, collector, pumping T, dc breaks, and output window. The measured reflection is a convolution of reflections from each of the transmission path elements and is basically

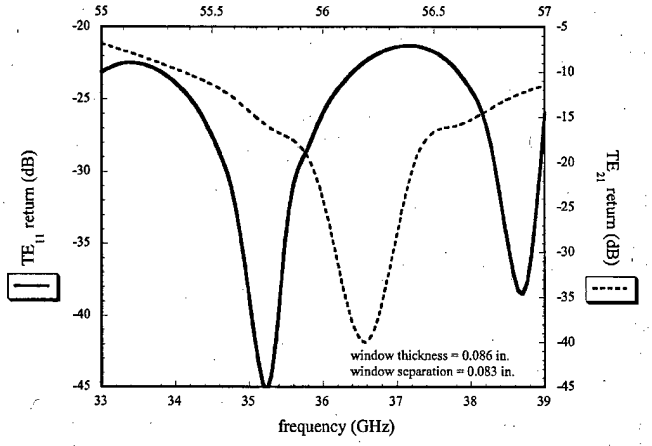

Fig. 6. Calculated window reflection for the TE_{11} and TE_{21} modes using measured dimensions.

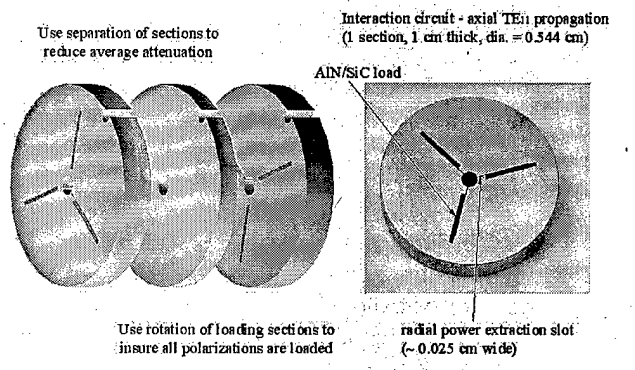

Fig. 7. TE_{11} mode distributed loss configuration. Loss sections are separated by unloaded sections to control attenuation and rotated to load all polarizations.

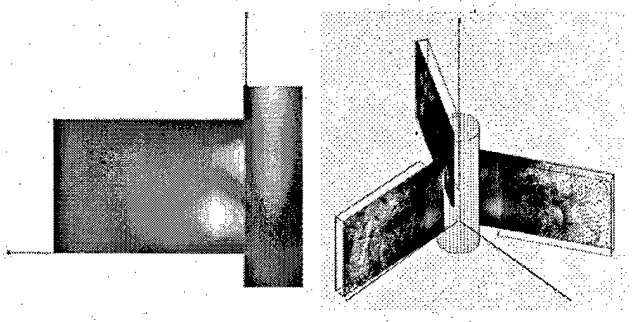

Fig. 8. Simulation results illustrating diffractive loss mechanism. (a) Time-averaged E field and (b) time snapshot of the radially extracted E field.

the reflection characteristic of the uptaper with superimposed ripples indicative of "long line" mismatches. The magnitude of these ripples is consistent with a window reflection for the TE_{11} mode of ~ -20 dB from 33 to 39 GHz.

4) Distributed Loss Design: The distinguishing feature of this amplifier design is the approach taken to attenuate the operating mode in a controlled manner over the majority of the interaction region. This loading configuration consists of multiple short, axially spaced sections, each of which has three thin axial slots equally spaced and azimuthally coupled to dielectric loads external to the interaction circuit [13]. Note that a somewhat similar slot-loading approach was employed in an earlier gyro-TWT, although with the primary goal of instability suppression and with only minimal impact to the operating mode [14]. The goals of the present loading configuration are as follows: 3.45-dB/cm attenuation of the TE_{11} operating mode with a frequency profile consistent with resistive wall loading (76-dB total attenuation over 22 cm), at least 4-dB/cm attenuation for the TE_{21} mode at 56 GHz and a multikilowatt average power capability.

The details of the configuration are a result of a somewhat complex tradeoff between several factors: slot width, slot length, number of slots, dielectric properties, and radial position of dielectric blocks affecting reflection characteristics. The slot width and number of slots control the gross attenuation and modes that can be attenuated. The addition of dielectric blocks to the walls of the slot "waveguides" introduces an impedance mismatch that is also dependent on slot width and length. This mismatch reflects a frequency-dependent fraction of the extracted power back into the interaction region, altering the net attenuation profile. In addition, the radial position of the dielectric magnifies the phase component of reflection that can alter the axial dependence of the attenuation profile.

We have chosen three slots as the minimum number of slots to load both polarizations of the operating TE_{11} and problematic TE_{21} modes. Additionally, the slot sections are spaced axially and rotated azimuthally. The slots are nominally 0.025-cm wide and are 2 cm in length. An illustration of the loading configuration is shown in Fig. 7.

This configuration is quite effective at loading the TE_{11} mode. In fact, very thin slots are required in order to prevent excessive loading. An illustration of the loading process is given in Fig. 8(a) and (b), showing the calculated E field amplitude reduction in the circular waveguide as the wave (a) propagates from top to bottom and (b) a time snapshot of the radially extracted E field with an incident circularly polarized TE_{11} wave. Note that the mag E profile is the same for each extraction slot. The load material is 80/20 AlN–SiC rather than the more conventional BeO–SiC. Note that HFSS design simulations used the dielectric constant for 80/20 AlN–SiC in K_a-band as measured by Calame [15]. Attenuation of the TE_{21} mode, as calculated using HFSS, is greater than 15 dB/cm, well above the requirement for stability.

5) Distributed Loss Characteristics: The measured attenuation and reflection characteristics are shown in Fig. 9 for disk assemblies from two manufacturers. Although the shapes of the attenuation profiles for the two assemblies are very similar, the measured average attenuations are somewhat different. These differences are due to the machining difficulty in achieving the desired slot widths. Attenuation for each case is normalized to 3.45 dB/cm at 35 GHz. In practice, this is achieved by inserting spacers or unloaded sections of the appropriate length between loaded sections. As a consequence of the additional spacers, the distributed loss configuration is no longer continuous but is more analogous to the TE_{01} loss configuration reported in [6] and has very little impact on amplifier performance, described below.

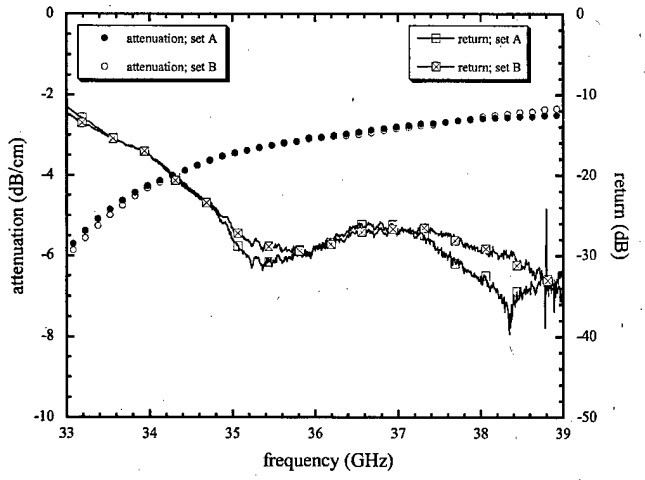

Fig. 9. Measured attenuation (normalized to decibels per centimeter) and reflection for two loading section sets.

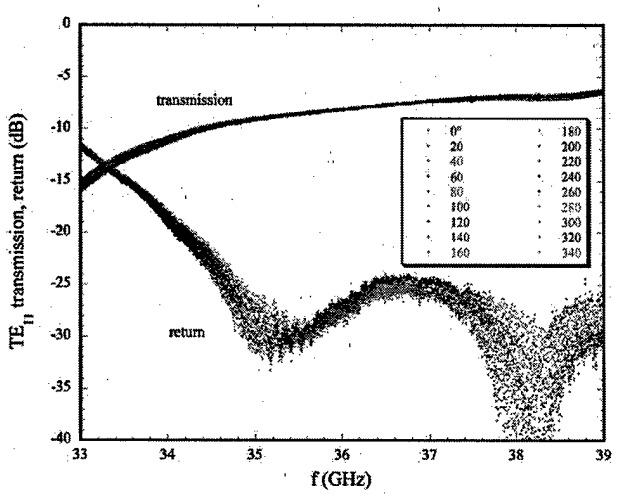

Fig. 10. Measured transmission and reflection for 2-cm-long slot. Loading is independent of polarization angle.

Consistent with calculations, note that the measured total attenuation and return do not depend on the angular orientation of the slots with respect to a linearly polarized input wave, as shown in Fig. 10. Since a spacer is typically required to normalize the attenuation to 3.45 dB/cm at 35 GHz, note also that the calculated attenuation characteristics are maintained with a spacer between the loading sections (Fig. 11), independent of polarization angle. Experimentally, there is no change in the transmission profile with the addition of a spacer.

Since it is necessary to include spacers to achieve the desired average attenuation, we have recalculated GTWT performance with the loading configuration consisting of alternating loaded and unloaded sections, using the measured frequency-dependent attenuation profiles for the disk assemblies. As shown in Fig. 12, there is practically no difference in the calculated amplifier performance with the discrete ("on/off") loading sections compared to continuous "resistive" type loading. The calculations were performed using MAGY [16], [17] for both "resistive" and "on/off" loading.

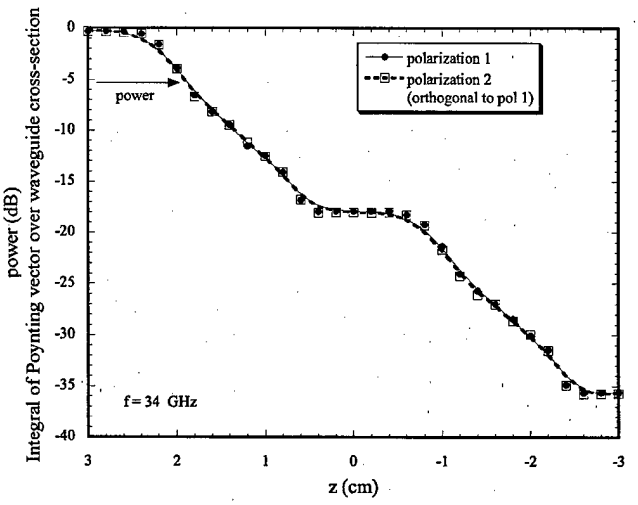

Fig. 11. Attenuation characteristics are maintained with a 1-cm separation between loaded sections, independent of incident polarization.

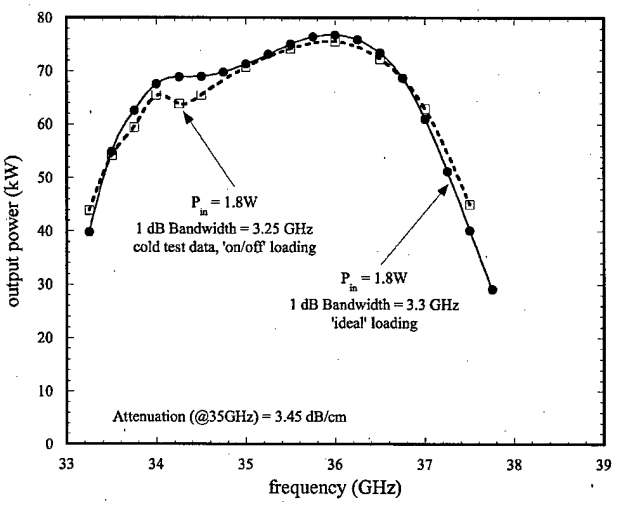

Fig. 12. Calculated gyro-TWT performance essentially the same for discrete separated loading sections as for continuous resistive type loading.

III. Experimental Results

This amplifier is the physical realization of the amplifier design described in [7]. The major performance characteristics delineated in that paper were: high gain, broadband amplification with output power dependent on both beam alpha (transverse/axial velocity ratio), and RF input power. We expect high gain and power with moderate bandwidth at "high" alpha (in this context, ~0.8), and lower gain, lower power with larger bandwidth with a lower alpha beam. More input power is required for saturation at low alpha. Also, for a given alpha, the bandwidth is dependent on input power. The flattest frequency response is obtained with the appropriate input power, slightly overdriven at low frequencies and underdriven at high frequencies. A somewhat limited series of experiments was performed that verified these characteristics.

Two measured bandwidth curves are shown in Figs. 13 and 14 with different magnetic field profiles and input powers for a 68-kV 6-A beam with 4% axial velocity spread. Typical beam

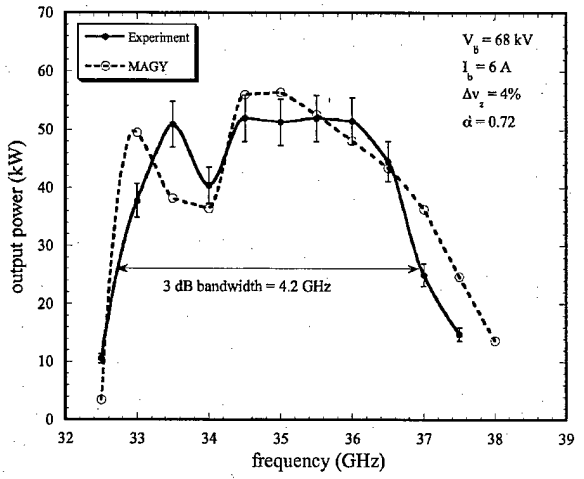

Fig. 13. Measured and calculated bandwidth for a 68-kV 6-A beam with 4% axial velocity spread and $\alpha = 0.72$. Magnetic field is tapered down over the interaction region. Magnetic field profile and the measured circuit loss characteristics are included in the simulations.

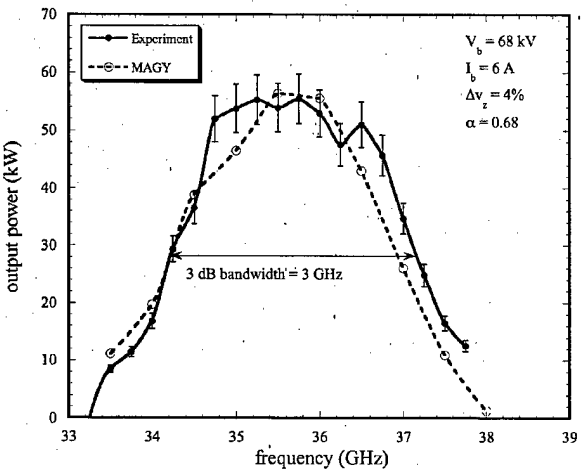

Fig. 14. Measured and calculated bandwidth for a 68-kV 6-A beam with 4% axial velocity spread and $\alpha = 0.68$. Magnetic field is flat over the interaction region. Magnetic field profile and the measured circuit loss characteristics are included in the simulations.

and RF pulse widths are 11 and 3 μs, respectively, at a pulse repetition rate of 3 pps. The nominal "flat" magnetic field magnitude is 12.1 kG. The 3-dB bandwidths range from 3 to 4 GHz (~9%–12%). MAGY simulation results are also shown for each parameter set for comparison. These simulations include the measured frequency-dependent attenuation profile of the loaded circuit, the z-dependent attenuation profile as discussed above, as well as the magnetic field profile. The agreement is quite good for both cases. Since we have no direct measurement of beam alpha, the values used for the MAGY simulations (~0.7) are estimated from EGUN [18] simulations using measured gun voltages and magnetic field profiles. Note that although a linearly polarized wave is used as input for the interaction, the RF output is circularly polarized, as expected, with equal power measured in orthogonal linear polarizations.

As a general characteristic, better performance, i.e., more power, is obtained with a tilted magnetic field profile that is higher upstream and lower downstream. The tilted profile is due to two factors, beam transmission and oscillation suppression. First, since the interaction circuit is relatively long, circuit alignment with the magnetic axis is critical for beam transmission. Better than 99.5% beam transmission was measured in initial operation at low alpha. However, due to a vacuum leak, the circuit was disassembled and removed from the magnet. After reassembly, it was found that a higher upstream field was required to eliminate body current for higher alpha beams. This is most likely due to misalignment between the mechanical and magnetic axes. Second, a lower magnetic field is required at the unloaded section to inhibit TE_{111} gyro-monotron oscillations, even for a flat field in the loaded section. This is probably due to higher than design reflections from the uptaper and downstream components, including window reflection. An improved uptaper would reduce this operational limitation. The magnetic field profile does complicate our interpretation of results, since the interaction is now z dependent as well as frequency dependent. Magnetic field profiles for these cases as well as the design profile are shown in Fig. 15.

By necessity, due to the beam transmission and oscillation issues discussed above, stable operation at the design magnetic field profile is only possible for a lower alpha beam. As shown in Fig. 16, this results in broad bandwidth at relatively low power. In this case, the design field profile is followed, except at the gun, where the field is somewhat higher, resulting in a lower alpha beam. The result using a tapered magnetic field with the same beam and RF parameters is also shown. In accordance with the expectations listed at the beginning of this section, the flatter magnetic field (lower alpha) results in lower power broader bandwidth operation.

Possibly a better example of power dependence on alpha is illustrated in Fig. 17, where "bandwidth" curves are shown for two values of the mod anode voltage within the same beam pulse. In this case, the magnetic field profile and RF input power remain constant, but the initial accelerating voltage increases during a beam pulse due to uncompensated capacitance in the modulator. In this figure, the output power versus frequency is plotted at the beginning and end of the RF pulse where the estimated alpha ranges from 0.7 to 0.73 due to the difference in mod anode voltage. With the exception of the lowest frequencies, the output power is reduced at lower alpha. It is likely that the higher alpha case is overdriven at low frequency for the given input power. There is an additional caveat in interpreting the figure as true bandwidth curves in that the input coupler was configured for circular polarization. As previously indicated, true circular polarization is only obtained near 36 GHz. As a consequence, the effective drive power is not constant with frequency. Note, that, with the same magnetic field profile at the interaction region, but with slightly less field at the gun (i.e., higher alpha) and higher drive power, a peak power of 78 kW was measured at 36 GHz. Representative beam voltage and current waveforms for this series are shown in Fig. 18, with the output detector waveforms at 33, 33.75, and 36 GHz overlaid. The output power variation during the pulse is clearly evident.

Bandwidth dependence on input power is illustrated in Fig. 19, where three bandwidth curves are shown with RF input power as a parameter. As the input power increases, lower frequencies are overdriven with a consequent reduction in output

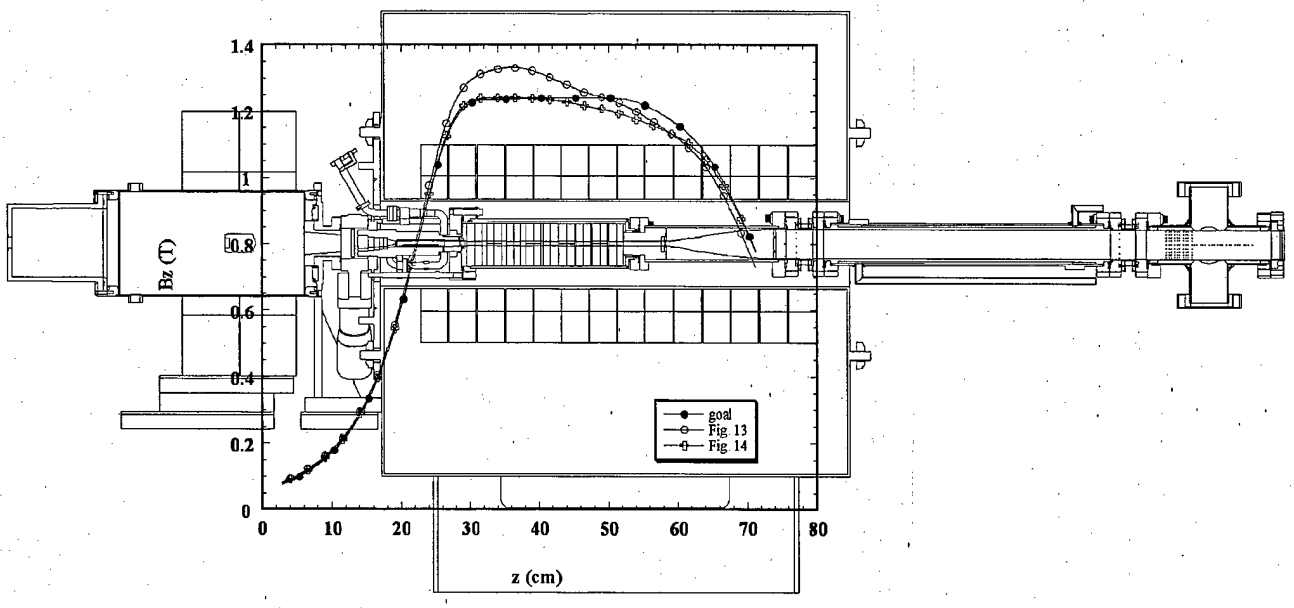

Fig. 15. Magnetic field profiles with circuit schematic. Design profile is shown, along with the tapered (Fig. 13) and flat (Fig. 14) profiles.

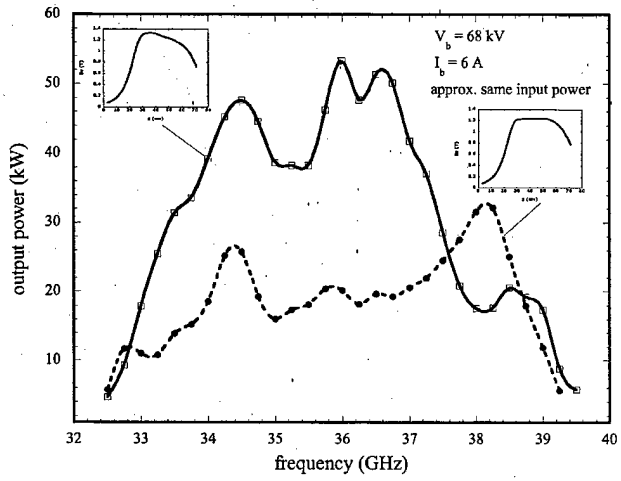

Fig. 16. Output power dependence on magnetic field profile.

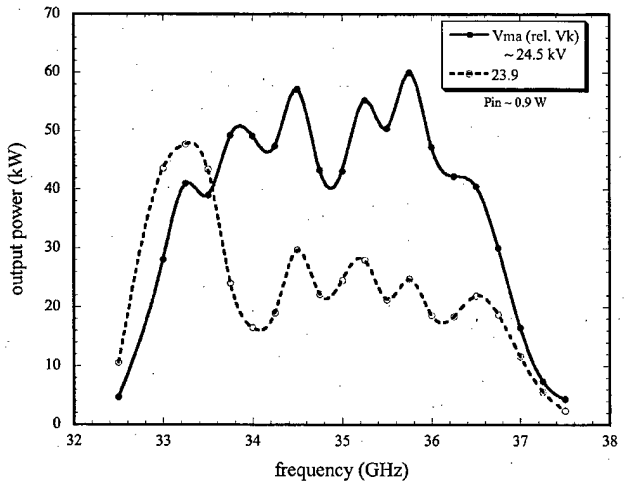

Fig. 17. Output power dependence on mode anode voltage and, hence, alpha.

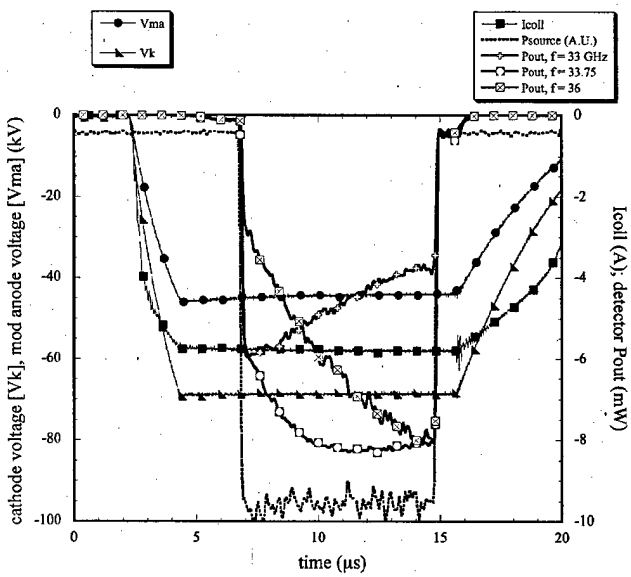

Fig. 18. Beam voltage, current, and detector output power waveforms. Note that Vma/Vk is not constant.

power, and the previously underdriven high frequencies now increase in power. As input power is increased, the effective "center" frequency shifts to higher frequencies.

Finally, to more explicitly demonstrate the wideband nature of interaction, the input power has been adjusted for saturated output at each frequency (Fig. 20). It must be emphasized that this is not a conventional bandwidth plot, but rather another illustration of the bandwidth potential of the gyro-TWT interaction. Clearly, the input power required for saturation increases from 33 to 39 GHz.

In general, the major calculated amplifier performance characteristics have been experimentally verified. High power and moderate bandwidth is obtained with a high alpha beam. Broader bandwidth at lower power is obtained with a lower

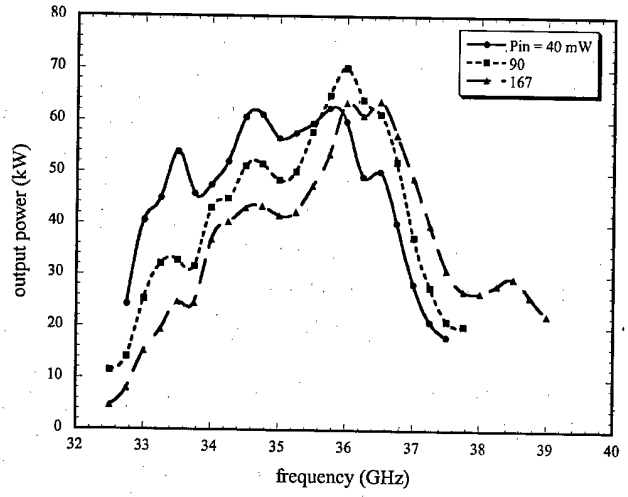

Fig. 19. Output power dependence on RF input power.

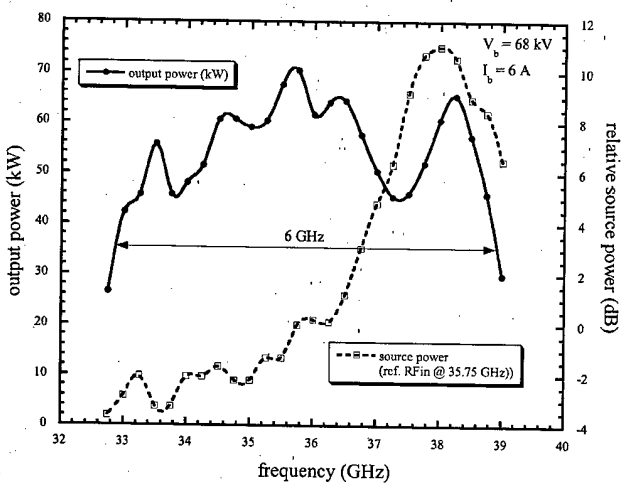

Fig. 20. Output driven to saturation at each frequency, illustrating the wideband potential of the interaction. This is not constant drive bandwidth. Relative source power is also plotted.

alpha beam and higher RF input power. The expected bandwidth dependence on RF input power was also observed. For this particular amplifier configuration, better results were obtained with a tapered magnetic field.

IV. Summary

Wideband high-power operation of a TE_{11} mode distributed loss gyro-TWT amplifier has been demonstrated in K_a-band. The 3-dB instantaneous bandwidths of 4.2 GHz at 52 kW have been measured with gains ~60 dB and efficiency ~12%. For different parameters, a peak power of 78 kW has been measured for an efficiency of 19%. The 3-dB saturated bandwidth at 70 kW is 6 GHz (17%), which is also the instantaneous bandwidth with appropriately tailored input power (e.g., gain equalizer). The measured performance is in good agreement with theoretical predictions. The efficacy of the distributed loss approach is apparent with the lack of parasitic oscillations; amplifier operation is zero-drive stable. Although this amplifier was operated at low duty, the loading configuration employed here is compatible with high-average power operation, needing only brazed ceramics and the addition of water cooling at the appropriate loading sections.

Acknowledgment

The authors would like to acknowledge the excellent technical support from R. Myers, F. Robertson, B. Sobocinski, G. Longrie, and D. Lobas.

References

[1] K. R. C. H.-Y. Chen, C.-L. Hung, T.-H. Chang, L. R. Barnett, S.-H. Chen, T.-T. Yang, and D. J. Dialetis, "Theory and experiment of ultrahigh gain gyrotron travelling wave amplifier," *IEEE Trans. Plasma Sci.*, vol. 27, pp. 391–404, 1999.

[2] D. B. McDermott, H. H. Song, Y. Hirata, A. T. Lin, L. R. Barnett, T. H. Chang, H.-L. Hsu, P. S. Marandos, J. S. Lee, K. R. Chu, and N. C. Luhmann, Jr, "Design of a W-band TE01 mode gyrotron traveling-wave amplifier with high power and broad-band capabilites," *IEEE Trans. Plasma Sci.*, vol. 30, pp. 894–902, June 2002.

[3] K. R. Chu, "Overview of research on the gyrotron traveling-wave amplifier," *IEEE Trans. Plasma Sci.*, vol. 30, pp. 903–908, June 2002.

[4] G. G. Denisov, V. L. Bratman, V. N. Manuilov, G. I. Kalynova, M. M. Ofitserov, S. B. Samsonov, and A. B. Volkov, *Dig. 27th Int. Conf. Infrared and Millimeter Waves*, Sept. 2002, pp. 197–198.

[5] J. P. Calame, M. Garven, B. G. Danly, B. Levush, and K. T. Nguyen, "Gyrotron-Traveling wave-tube circuits based on lossy ceramics," *IEEE Trans. Electron Devices*, vol. 49, pp. 1469–1477, Aug. 2002.

[6] M. Garven, J. P. Calame, B. G. Danly, K. T. Nguyen, D. E. Pershing, B. Levush, F. N. Wood, and D. E. Pershing, "A gyrotron-traveling-wave tube amplifier experiment with a ceramic loaded interaction region," *IEEE Trans. Plasma Sci.*, vol. 30, pp. 886–894, June 2002.

[7] K. T. Nguyen, J. P. Calame, D. E. Pershing, B. G. Danly, M. Garven, B. Levush, and T. M. Antonsen, "Design of a Ka-band gyro-TWT for radar applications," *IEEE Trans. Electron Devices*, vol. 48, pp. 108–115, Jan. 2001.

[8], Ansoft Corporation.

[9] D. E. Pershing, R. D. Seeley, R. H. Jackson, and H. P. Freund, "Amplifier performance of the NRL ubitron," *Nucl. Instrum. Methods Phys. Res.*, vol. A 358, pp. 104–107, 1995.

[10] , Calabazas Creek Research, Inc..

[11] J. M. Neilson, P. E. Latham, M. Caplan, and W. Lawson, *IEEE Trans. Microwave Theory Tech.*, vol. 37, pp. 1165–1170, 1989.

[12] G. Armand and J. Lapujoulade, "Liaisons quartz metal etuvables,", Le Vide No 105, 1963.

[13] D. E. Pershing, J. P. Calame, K. T. Nguyen, B. G. Danly, and B. Levush, "A distributed loss technique for high average power gyro-TWTs," in *Proc. 2nd Int. Vacuum Electronics Conf.*, Noordwijk, The Netherlands, Apr. 2001, pp. 145–146.

[14] Q. S. Wang, D. B. McDermott, and N. C. Luhmann Jr, "Operation of a stable 200 kW second-harmonic gyro-TWT amplifier," *IEEE Trans. Plasma Sci.*, vol. 24, pp. 700–706, June 1996.

[15] J. P. Calame, D. K. Abe, B. Levush, and B. G. Danly, "Variable temperature measurements of the complex dielectric permittivity of lossy ALN-SiC composites from 26.5–40 GHz," *J. Appl. Phys.*, vol. 89, no. 10, pp. 5618–5621, May 2001.

[16] K. T. Nguyen, B. Levush, T. M. Antonsen Jr, M. Botton, M. Blank, J. P. Calame, and B. G. Danly, "Modeling of gyroklystrons with MAGY," *IEEE Trans. Plasma Sci.*, vol. 28, pp. 867–886, June 2000.

[17] M. Botton, T. M. Antonsen Jr, B. Levush, K. T. Nguyen, and A. N. Vlasov, "MAGY: A time-dependent code for simulation of slow and fast microwaves devices," *IEEE Trans. Plasma Sci.*, vol. 26, pp. 882–882, 1998.

[18] W. B. Herrmannsfeldt, "Numerical design of electron guns and space charge limited transport systems,", SLAC Rep. SLAC-PUB-2631, 1980.

Dean E. Pershing received the B.S. and the Ph.D. degrees in physics from North Carolina State University in 1971 and 1980, respectively.

In 1980, he continued research on the generation and propagation of intense electron and ion beams as a NRC/NRL Post-doctoral Research Associate while participating in the Naval Research Laboratory Ion Ring Program. From 1981 to 1983, he participated in the design of the Modified Betatron Accelerator at NRL, while a staff member of JAYCOR. Since joining Mission Research Corporation, Newington, VA, in 1983, his research interests have included the design and testing of high-power microwave amplifiers, including ubitron/FELs and, most recently, gyroklystrons, gyroTWTs, and multiple beam klystrons.

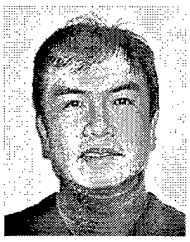

Khanh T. Nguyen received the B.S. degree in physics and mathematics in 1978, the M.S. degree in mathematics in 1979, and the M.S. and Ph.D. degrees in nuclear science in 1980 and 1983, respectively, all from the University of Michigan, Ann Arbor.

He then joined the Department of Research and Technology, Naval Surface Warfare Center, White Oak, where he was the Lead Theorist for the charged particle beam propagation experimental program. In 1989, he joined the Washington Office of Mission Research Corporation (MRC) as a Senior Scientist, and later became the Leader of the Electromagnetic Application Group. At MRC, his research interests included the areas of charged particle beam propagation, vacuum electronics, compact accelerator development, X-ray and γ-ray simulators, and high-power microwave source development. Since 1994, he has been associated with the Vacuum Electronics Branch, Naval Research Laboratory, as an on-site Contractor. He is presently the President of Beam-Wave Research, Inc. His current research includes the design and modeling of vacuum electronic devices.

Jeffrey P. Calame (M'96) received the B.S., M.S., and Ph.D. degrees, all in electrical engineering, from the University of Maryland, College Park, in 1985, 1986, and 1991, respectively.

Presently he is employed at the Naval Research Laboratory, Washington, DC, where he is developing high average power, wideband millimeter wave amplifiers for radar applications and studying the dielectric, ac magnetic, and thermal properties of composite ceramic materials. He is also performing research on high heat flux cooling techniques.

Dr. Calame received the 1991 APS award for outstanding doctoral thesis research in beam physics.

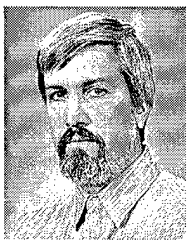

Bruce G. Danly received the B.A. degree in physics from Haverford College in 1978 and the Ph.D. degree in physics from the Massachusetts Institute of Technology (MIT), Cambridge, in 1983.

From 1983 to 1995, he was on the research staff at the MIT Plasma Fusion Center, first as a Research Scientist from 1983 to 1992 and then as a Principal Scientist from 1992 to 1995. While at MIT, he participated in research on gyrotrons, free-electron lasers, relativistic klystrons, and other high-power RF source technologies for use in plasma heating and high-gradient RF linear accelerators. In 1995, he joined the Naval Research Laboratory (NRL)Washington, DC, as Head of the High Power Devices Section, Vacuum Electronics Branch, in the Electronics Science and Technology Division. The high-power devices section carries out experimental research and development on new concepts for high power microwave, millimeter wave, and infrared sources based on both slowwave and fastwave interaction mechanisms and on improvements in existing technology to meet new requirements. Technologies he investigates include gyrotron amplifiers (gyroklystrons, gyrotwystrons, gyro-TWTs), free-electron lasers, TWTs, and klystrons. His current research interests include high-power millimeter wave gyro-amplifiers and nonlinear distortion and memory effects in TWTs used in high data rate communication systems.

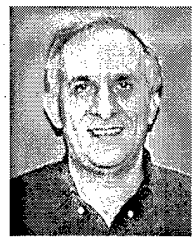

Baruch Levush (M'88–SM'90–F'01) received the M.Sc. degree in physics from Latvian University, Riga, Latvia, and the Ph.D. degree in physics from Tel-Aviv University, Tel-Aviv, Israel.

In 1985, he joined the Institute of Plasma Research, University of Maryland, College Park, where his research has focused on the physics of coherent radiation sources and the design of high power microwave sources, such as gyrotrons, traveling-wave tubes, backward-wave oscillators, and free-electron lasers. In 1995, he joined the Naval Research Laboratory, Washington, DC, as Head of the Theory and Design Section of the Vacuum Electronics Branch, Electronics and Technology Division. He is actively involved in developing theoretical models and computational tools for analyzing the operation of existing microwave vacuum devices and in inventing new concepts for high-power, high frequency coherent radiation sources. He is responsible for developing a suite of new design codes for vaccum electron devices under the auspices of the Office of Naval Research Modeling and Simulation project. He is the coauthor of over 140 journal articles.

Dr. Levush was the recipient of the 1999 Robert L. Woods Award for his role in the successful development of a 10-kW average power, W-band gyroklystron.

Franklin N. Wood received the B.S. degree in mechanical engineering from George Washington University, Washington, DC, in 1983.

He has been involved in the design of high-power microwave tubes and ancillary experimental equipment since 1983. In the Vacuum Electronics Branch of the Electronics Science and Technology Division, Naval Research Laboratory (NRL) he is designing high-power, broadband gyroklystrons and gyro-TWTs as a Contractor from Mission Research Corporation. He worked with the Universities Research Associates, Dallas, TX, under contract to the Department of Energy, from 1990 to 1994, on the design and fabrication of a proton accelerator for the superconducting super collider.

M. Garven, photograph and biography not available at the time of publication.